

Realization of Highly Efficient Red Phosphorescence from Bis-Tridentate Iridium(III) Phosphors

Premkumar Gnanasekaran,^{†,⊥} Yi Yuan,^{‡,§,⊥} Chun-Sing Lee,^{‡,*} Xiuwen Zhou,^{*,||} Alex K.-Y. Jen,^{*,‡} and Yun Chi^{*,†,‡}

[†]Department of Chemistry and Frontier Research Center on Fundamental and Applied Sciences of Matters, National Tsing Hua University, Hsinchu 30013, Taiwan

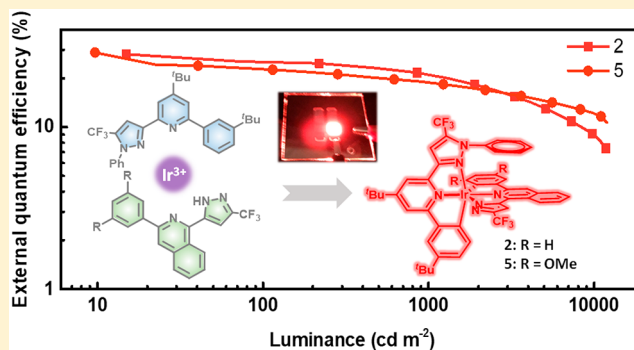
[‡]Department of Materials Science and Engineering and Department of Chemistry, City University of Hong Kong, Kowloon, Hong Kong SAR

[§]Center of Super-Diamond and Advanced Films (COSDAF), City University of Hong Kong, Kowloon, Hong Kong SAR

^{||}School of Mathematics and Physics, The University of Queensland, Brisbane, Queensland 4072, Australia

Supporting Information

ABSTRACT: Bis-tridentate Ir(III) metal complexes bring forth interesting photophysical properties, among which the orthogonal arranged, planar tridentate chelates could increase the emission efficiency due to the greater rigidity and, in the meantime, allow strong interligand stacking that could deteriorate the emission efficiency. We bypassed this hurdle by design of five bis-tridentate Ir(III) complexes (1–5), to which both of their monoanionic ancillary and dianionic chromophoric chelate were functionalized derivative of 2-pyrazolyl-6-phenylpyridine, i.e. pzppyph₂ parent chelate. Hence, addition of phenyl substituent to the pyrazolyl fragment of pzppyph₂ gave rise to the precursors of monoanionic chelate (A1H–A3H), on which the additional *tert*-butyl and/or methoxy groups were introduced at the selected positions for tuning their steric and electronic properties, while precursors of dianionic chelates was judiciously prepared with an isoquinolinyl central unit on pziqph₂ in giving the red-shifted emission (cf. L1H₂ and L2H₂). Factors affected their photophysical properties were discussed by theoretical methods based on DFT and TD-DFT calculation, confirming that the T₁ excited state of all investigated Ir(III) complexes shows a mixed metal-to-ligand charge transfer (MLCT), intraligand charge transfer (ILCT), ligand-to-ligand charge transfer (LLCT), and ligand-centered (LC) transition character. In contrast, the poor quantum yield of 3 is due to the facilitation of the nonradiative decay in comparison to the radiative process. As for potential OLED applications, Ir(III) complex 2 gives superior performance with max. efficiencies of 28.17%, 41.25 cd·A⁻¹ and 37.03 lm·W⁻¹, CIE_{x,y} = 0.63, 0.37 at 50 mA cm⁻², and small efficiency roll-off.



1. INTRODUCTION

Organic light emitting diodes (OLEDs) have been considered as the emerging technology for flat panel displays and solid-state luminaries of the 21st century. Since the first report on electroluminescence,¹ the OLED emitters have evolved from fluorescent² and phosphorescent^{3–8} ultimately to thermally activated delayed fluorescent (TADF).^{9–13} Among these three generations of designs, the fluorescent materials utilize only the singlet excitons, which set the highest possible internal quantum efficiency to only 25%. In contrast, both the phosphorescent and TADF emitters take advantage of the fast (both forward and reversed) intersystem crossing induced by the inherent heavy atom effect as well as the small gap between the singlet and triplet excited states, which, in theory, give a unitary internal quantum efficiency for the fabricated OLED devices. Nowadays, the blue fluorescent emitter and

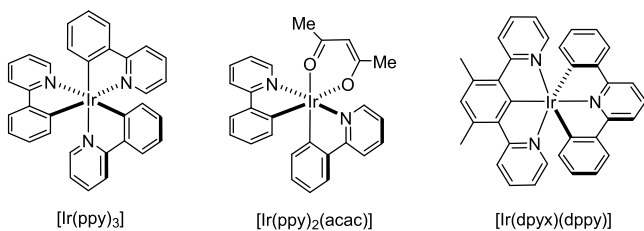
green and red phosphors have all been used for commercial OLED devices, while corresponding TADF emitters are considered as the future replacements.

Moreover, all these OLED emitters required good stability to survive the harsh condition applied during electrical excitation, which remained to be the central focus in this arena. In this regard, for the phosphorescent emitters, changing the traditional design, cf. Ir(III) complexes with three bidentate chelates (tris-bidentate), to those with only two tridentate chelates (bis-tridentate) would offer the respective phosphors with improved stability due to the multidentate coordination nature of chelates.¹⁴ To date, the tris-bidentate Ir(III) phosphors are common; for example, homoleptic

Received: May 12, 2019

[Ir(ppy)₃] and heteroleptic [Ir(ppy)₂(acac)] have been considered as the excellent dopants for various monochromatic and white-emitting OLED applications (cf. Scheme 1).^{15,16} On

Scheme 1. Drawings of Ir(III) Complexes [Ir(ppy)₃], [Ir(ppy)₂(acac)], and [Ir(dpyx)(dppy)]

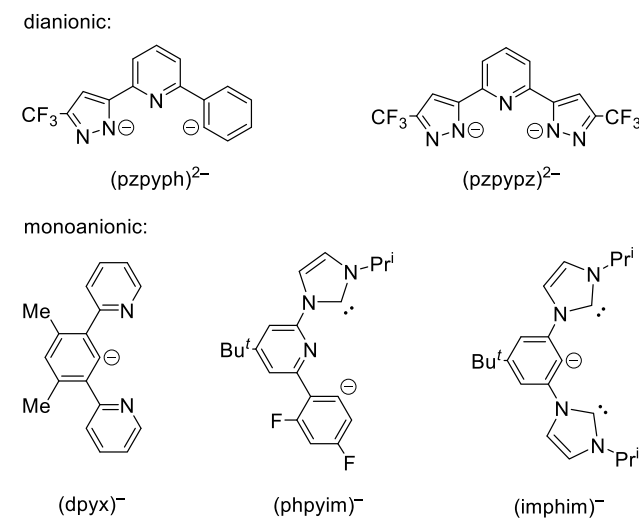


the other hand, the best known example of bis-tridentate Ir(III) complex is [Ir(dpyx)(dppy)], bearing chelates derived from 1,3-di(2-pyridyl)-4,6-dimethylbenzene (dpyx)H and 2,6-diphenylpyridine (dppy)H₂, despite poor luminescent efficiency.^{17,18} In fact, the design challenge in bis-tridentate complexes lies on how to control the energy gap and inherent properties of luminescent metal complexes, which are deemed necessary for device fabrication using vacuum deposition. The next endeavor is finding a high yield route to incorporate these tailor-made tridentate chelates (both monoanionic and dianionic) around the Ir(III) metal center in a systematic fashion.^{19,20}

Recently, we have described utilization of the precursors of dianionic tridentate chelates with one or two pyrazolyl units (cf. pzpyphH₂ and pzpyzH₂) in synthesizing the bis-tridentate Ru(II), Os(II), and Ir(III) complexes.^{20,21} Our examinations hinted that, independent to the central metal atoms, it is essential to first incorporate a neutral or monoanionic chelate to the employed metal reagents, followed by addition of dianionic chelate in affording the bis-tridentate arrangement. This strategic sequence is important as the first added chelate with less negative charge will coordinate to the metal reagents in giving intermediate of high synthetic yield. For instance, 2,2':6,2''-terpyridine (tpy) and functional chelates reacted with MCl₃, M = Ru and Os, in giving [(tpy)MCl₃], which can convert to the bis-tridentate complexes upon addition of functional derivatives of pzpyphH₂ and pzpyzH₂, affording excellent sensitizers suited for making dye-sensitized solar cells (DSSC).^{22–25} Moreover, the bis-tridentate Ir(III) complexes [Ir(dpyx)(dppy)] and [Ir(fpby)(dppy)] were known to be produced by first treatment of IrCl₃·3H₂O with (dpyx)H or 6-(5-trifluoromethylpyrazol-3-yl)-2,2'-bipyridine (fpby)H in giving isolable dimer complex [Ir(dpyx)(μ-Cl)Cl]₂ or hypothetical [Ir(fpby)(μ-Cl)Cl]₂, followed by conversion to the bis-tridentate complexes [Ir(dpyx)(dppy)] and [Ir(fpby)(dppy)] upon addition of (dppy)H₂.^{17,26} In fact, this sequential transformation remained useful for other monoanionic chelates with imidazolium carbene unit, i.e., phpyim[−] and impyim[−] (Scheme 2), which are the key ancillaries in giving efficient blue-emitting bis-tridentate Ir(III) phosphors.^{27–29}

With this motivation, we proceed to investigate the bis-tridentate Ir(III) complexes bearing monoanionic chelate such as pz^{Ph}pyph[−] and functional analogues. We anticipated that addition of a phenyl substituent to the peripheral pyrazolate of pzpyphH₂ in giving pz^{Ph}pyphH as shown in Scheme 3 should convert the corresponding tridentate chelate from dianionic to

Scheme 2. Structural Drawings of Dianionic Chelates, pzpyph^{2−} and pzpyz^{2−}, and Monoanionic Chelates, dpyx[−], phpyim[−], and impyim[−], Respectively



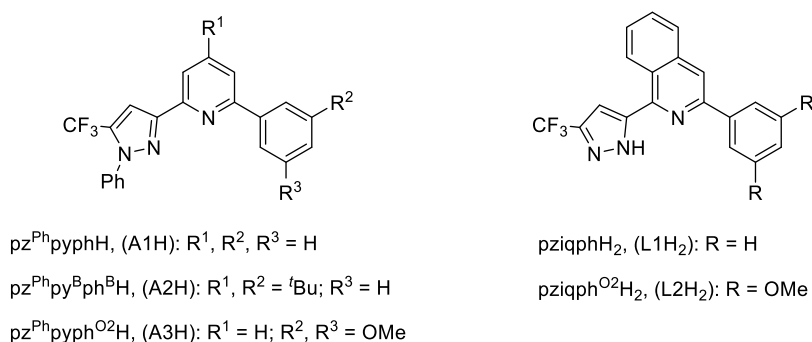
monoanionic due to removal of the pyrazolic NH fragment. Hence, a total of three functional designs (cf. A1H–A3H) were introduced, with an aim to probe both the steric and electronic effects imposed by the introduced substituents. Furthermore, the second tridentate chelate precursors are also prepared using a central isoquinolinyl entity for reducing the ligand-centered ππ* (or intraligand charge transfer, ILCT) energy gap and giving efficient red emission, i.e., L1H₂ and L2H₂. Preparation of the bis-tridentate Ir(III) emitters was next conducted using the literature strategy. From the viewpoint of molecular design, this work represents an interesting example on the bis-tridentate Ir(III) phosphors with chelate deriving from essentially identical origin. Hence, these Ir(III)-based materials could enrich the prospective of OLED emitters with high efficiency.

2. RESULTS AND DISCUSSION

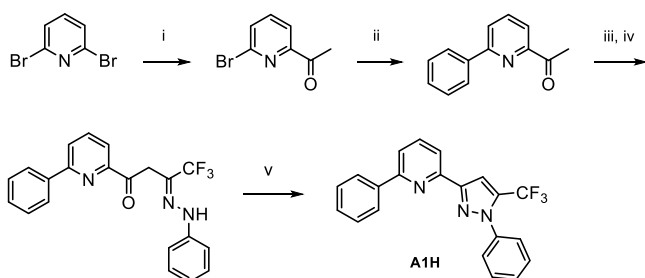
2.1. Synthesis and Characterization. All needed tridentate chelates for this investigation are summarized in Scheme 3. They consist of both the monoanionic ancillaries An[−] (n = 1–3) and dianionic chelates Ln^{2−} (n = 1 and 2); the latter possesses a relatively smaller ligand-centered ππ* or ILCT energy gap in comparison to that of An[−] ancillaries, attributed to the replacement of central pyridyl unit in An[−] with the isoquinolinyl fragment in Ln^{2−} with greater π-conjugation. It is interesting to note that both the tridentate An[−] and Ln^{2−} chelates are derived from the original design of pzpyphH₂.

The precursor of N-phenyl-substituted ancillary chelate, pz^{Ph}pyphH (A1H), was synthesized using a multistep protocol depicted in Scheme 4. First, 2,6-dibromopyridine was treated with n-BuLi, followed by addition of N,N-dimethyl acetamide at −78 °C in affording 2-acetyl-6-bromopyridine, which was next coupled with phenylboronic acid to yield 2-acetyl-6-phenylpyridine. Subsequent Claisen condensation of 2-acetyl-6-phenylpyridine with ethyl trifluoroacetate produced a diketone intermediate that, in turn, underwent reaction with phenyl hydrazine and, next, with acid-catalyzed hydrazone cyclization to afford the desired precursor A1H. Analogously, two more precursors of functional ancillaries, namely pz^{Ph}py^Bph^BH (A2H) and pz^{Ph}pyph^{O₂H} (A3H), one with a

Scheme 3. Structural Drawings of the Studied Precursors of Chelates, pzpyphH (AnH), $n = 1-3$, and pziqphH₂ (LnH_2), $n = 1$ and 2



Scheme 4. Synthetic Protocols to $pz^{Ph}pyphH$ (A1H) Chelate^a



^aExperimental conditions: (i) *n*-BuLi, dimethylacetamide, diethyl ether; (ii) phenyl boronic acid, Pd(dppf)Cl₂, K₂CO₃, toluene:water:ethanol (7:1.5:1.5), reflux; (iii) NaOEt, ethyl trifluoroacetate, THF, reflux; (iv) phenyl hydrazine, *p*-TsOH·H₂O, ethanol, reflux; (v) concentrated HCl, ethanol, reflux.

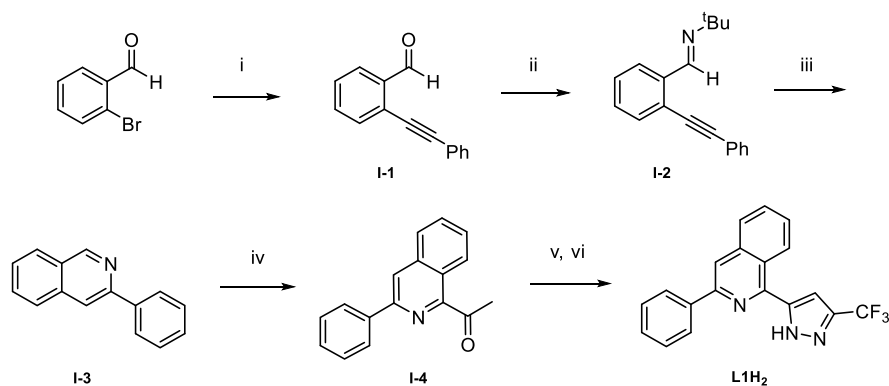
tert-butyl group located at both the central pyridyl and peripheral phenyl units and the second with the 3,5-dimethoxy substituted peripheral phenyl group for adjusting electronic properties, were prepared using relevant starting materials, following the analogous procedures depicted in Scheme 4.

Next, synthesis of 3-phenyl-1-(3-(trifluoromethyl)-1*H*-pyrazol-5-yl) isoquinoline, pziqphH₂ (L1H₂) is depicted in Scheme 5, to which the procedures are slightly more complicated than those described for the precursors of monoanionic An^- ancillaries, as needed for construction of

central isoquinolinyl unit. Hence, Sonogashira cross-coupling was first employed to link 2-bromobenzaldehyde and phenylacetylene in forming 2-(phenylethynyl)benzaldehyde (I-1),³⁰ which was treated with *t*-butylamine in affording *N*-*tert*-butyl-1-(2-(phenylethynyl)phenyl)methanimine (I-2).³¹ Cyclization of I-2 in the presence of CuI afforded the 3-phenylisoquinoline (I-3), to which the catalytic acylation with paraldehyde afforded 1-(3-phenylisoquinolin-1-yl)ethan-1-one (I-4). Subsequently, this acetyl isoquinoline derivative undergoes Claisen condensation with ethyl trifluoroacetate in giving the diketone intermediate, to which the hydrazine cyclization afforded the 3-phenyl-1-(3-(trifluoromethyl)-1*H*-pyrazol-5-yl)isoquinoline (L1H₂). The 3,5-dimethoxy substituted pziqph^{OMe}H₂ (L2H₂) was obtained in a similar fashion, which is expected to have an even more reduced $\pi\pi^*$ energy gap compared to that of the parent precursor L1H₂.

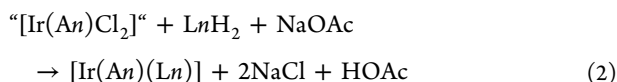
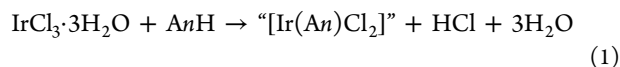
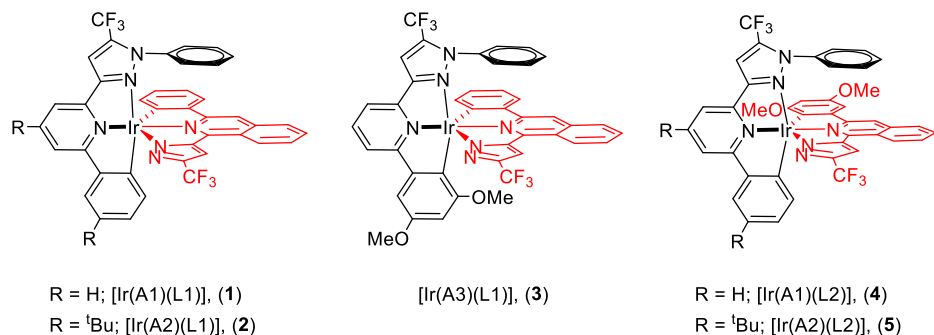
With both chelates in hands, the demanded bis-tridentate Ir(III) complexes 1–5 were obtained by first treatment of one equiv of AnH (i.e., A1H–A3H) with IrCl₃·3H₂O in refluxing ethanol for 12 h. After that, the ethanol was removed under vacuum to afford a residue. To this uncharacterized material were added an equal molar ratio of the second chelating precursors LnH_2 (i.e., L1H₂ and L2H₂), an excess of sodium acetate as catalyst, and decalin as solvent. The resulting mixture was heated to reflux for 48 h, to which the stepwise transformations are depicted below:

Scheme 5. Synthetic Protocols to pziqphH₂ (L1H₂) Chelate^a



^aExperimental conditions: (i) phenyl acetylene, Pd(PPh₃)₂Cl₂, CuI, dry Et₃N, 50 °C; (ii) *tert*-butylamine, room temperature; (iii) CuI, DMF, 100 °C; (iv) FeSO₄·7H₂O, paraldehyde, CF₃CO₂H, *t*-BuO₂H, CH₃CN, reflux; (v) NaOEt, ethyl trifluoroacetate, THF, reflux; (vi) hydrazine hydrate, *p*-TsOH·H₂O, ethanol, reflux.

Scheme 6. Structural Drawings of the Studied Bis-Tridentate Ir(III) Metal Complexes 1–5



Upon chromatographic separation and recrystallization, the expected charge-neutral bis-tridentate Ir(III) complexes with general formula $[\text{Ir}(\text{An})(\text{Ln})]$ were isolated in moderate to high yields. Scheme 6 presents the molecular drawings of these Ir(III) complexes. It is also notable that two Ir(III) complexes 2 and 5, both with two *tert*-butyl substituted ancillary A2[−], tend to afford the best product yields of >80%, in comparison to other ancillary (i.e., A1[−] and A3[−]) without the *tert*-butyl substituent (39 ~ 45%). It is expected that the *tert*-butyl substituents of A2H can block the unwanted side reactions, particularly on the central pyridinyl unit, and giving better yields in comparison to those using precursors A1H and A3H. After then, these Ir(III) complexes were characterized by ¹H and ¹⁹F NMR spectroscopic methods, mass spectrometry, and elemental analyses.

Single crystal X-ray analyses of Ir(III) complex 1, i.e. $[\text{Ir}(\text{A1})(\text{L1})]$, were also conducted to reveal their true identity. As shown in Figure 1, both the tridentate A1[−] and L1^{2−} chelates are coordinated to the central Ir(III) atom in a mutually orthogonal fashion, to which the overall molecular arrangement resemble that of the homoleptic bis-tridentate Ir(III) complexes reported earlier.³² The dianionic chelate L1 has C(22)–Ir–N(5) bite angle of ~159° and isoquinolinyl Ir–N(4) distance of 2.001(2) Å, the latter is much shorter compared to the adjacent pyrazolyl Ir–N(5) distance of 2.092(2) Å and Ir–C(22) distance of 2.020(2) Å. Similarly, an C(1)–Ir–N(2) bite angle of ~157° was also observed for monoanionic A2[−] ancillary, except the existence of a lengthened pyrazolyl Ir–N(2) distance of 2.154(2) Å due to the attachment of N-phenyl substituent. Finally, this phenyl appendage from A1[−] chelate is perfectly residing over the isoquinolinyl ring of L1^{2−} chelate, showing notable through-space π – π interaction. The calculated center-to-center distance between the phenyl and isoquinolinyl group is approximately 3.648 Å, coinciding to those of π – π stacking distances reported in relevant supramolecularly caged Ir(III) complexes.^{33–38}

2.2. Photophysical Properties. The UV–visible absorption and emission spectra of the bis-tridentate Ir(III) complexes 1–5 in CH₂Cl₂ solution were shown in Figure 2, and photophysical data were depicted in Table 1. The intense absorptions from 340 to 450 nm with relatively higher extinction coefficient are contributed mainly by $\pi\pi^*$ transitions

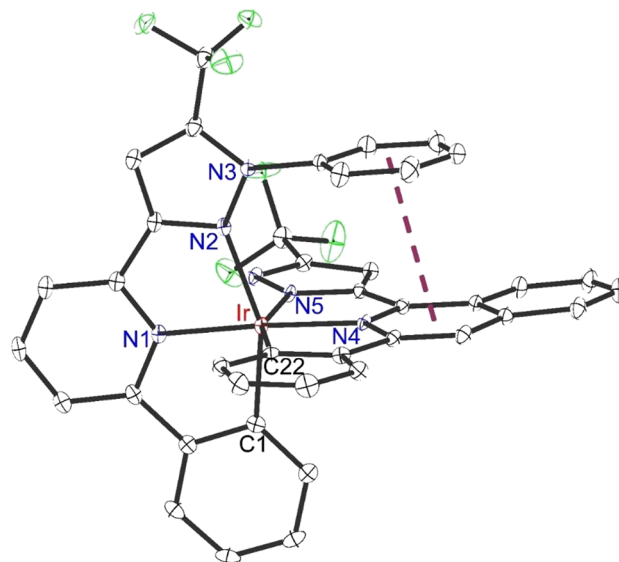


Figure 1. Structural drawing of 1 with thermal ellipsoids shown at the 30% probability level. Selected bond distances: Ir–C(1) = 2.005(2), Ir–C(22) = 2.020(2), Ir–N(1) = 2.000(2), Ir–N(2) = 2.154(2), Ir–N(4) = 2.001(2), and Ir–N(5) = 2.092(2) Å. Bond angles: C(1)–Ir–N(2) = 157.31(8), C(22)–Ir–N(5) = 159.26(8), and N(1)–Ir–N(4) = 176.51(8)°.

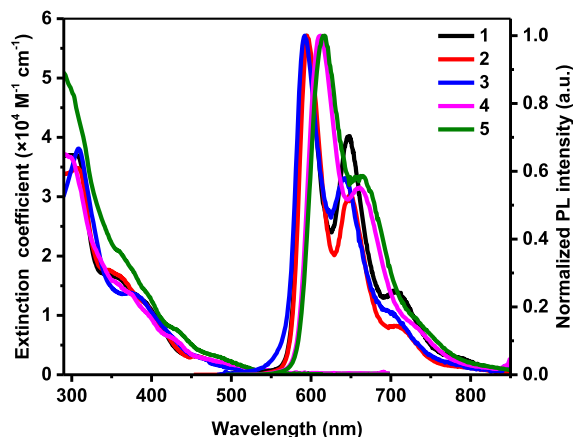


Figure 2. Absorption and emission spectra of Ir(III) complexes 1–5 recorded in CH₂Cl₂ at room temperature.

within 2-(1-phenyl-pyrazolyl)-6-phenyl pyridine (An[−]) ancillary and 1-pyrazolyl-3-phenyl isoquinoline chromophoric chelate (Ln^{2−}). The broadened absorption centered at around 475 nm was attributed to the spin-allowed metal-to-ligand charge

Table 1. Absorption and Emission Properties of Ir(III) Complexes 1–5 Recorded in CH₂Cl₂ at Room Temperature

	abs λ [nm] ($\epsilon \times 10^{-4} \text{ M}^{-1}\text{cm}^{-1}$) ^a	em λ_{max} [nm] ^b	Φ [%] ^{b,c}	τ_{obs} [μs]	k_{r} [$\times 10^5 \text{ s}^{-1}$]	k_{nr} [$\times 10^5 \text{ s}^{-1}$]
1	254 (4.68), 301 (3.7), 345 (1.7), 452 (0.31)	593, 645, 704	98	7.42	1.31	0.026
2	253 (4.55), 307 (3.48), 346 (1.76), 454 (0.308)	595, 649, 707	100	6.19	1.61	–
3	308 (3.81), 373 (1.38), 470 (0.25)	592, 643, 705	15	0.69	2.2	12
4	290 (3.72), 375 (1.36), 470 (0.26)	612, 661, 735	90	4.46	2.01	0.22
5	290 (5.09), 358 (2.09), 476 (0.33)	617, 666, 735	100	3.74	2.7	–

^aAll absorption spectra were measured using a 10^{-5} M of CH₂Cl₂ solution at room temperature; ^bEmission spectra were measured in degassed CH₂Cl₂ solution at room temperature. ^c4-Dicyanomethylene-2-methyl-6-(4-dimethylaminostyryl)-4H-pyran in DMSO (Q.Y. = 80% and $\lambda_{\text{max}} = 637 \text{ nm}$), which was employed as a standard.

Table 2. Electrochemical and Energy Gap Data of Studied Ir(III) Complexes 1–5

	Measurement				DFT ^c			
	$E_{1/2}^{\text{ox}}$ [V]	$E_{1/2}^{\text{red}}$ [V]	HOMO ^b [eV]	optical gap ^c [eV]	LUMO ^d [eV]	HOMO [eV]	LUMO [eV]	H–L gap [eV]
1	0.53 [0.10]	–2.30 [0.10]	–5.33	2.17	–3.16	–5.47	–1.84	3.63
2	0.46 [0.13]	–2.38 [0.12]	–5.26	2.17	–3.09	–	–	–
3	0.30 [0.07]	–2.32 [0.09]	–5.10	2.21	–2.89	–5.20	–1.76	3.44
4	0.27 [0.14]	–2.37 [0.11]	–5.07	2.14	–2.93	–5.18	–1.82	3.36
5	0.25 [0.21]	–2.42 [0.12]	–5.05	2.13	–2.92	–	–	–

^a $E_{1/2}$ refers to $(E_{\text{pa}} + E_{\text{pc}})/2$, where E_{pa} and E_{pc} are the anodic and cathodic potentials, respectively, referenced to the redox couple ($\text{Fc}/\text{Fc}^+ = -4.8 \text{ eV}$), while the corresponding values of $\Delta E_{\text{p}} = E_{\text{pa}} - E_{\text{pc}}$ are given in square brackets. The oxidation wave and reduction wave measured in CH₂Cl₂ and THF solution, respectively. ^bHOMO = $-(E_{\text{ox}} + 4.8) \text{ eV}$. ^cOptical gap (eV) = 1240/phosphorescent onset (nm). ^dLUMO = HOMO + optical gap. ^ePBE1PBE/6-31G** (LANL2DZ with ECP for Ir) level with PCM for modeling the CH₂Cl₂ solvent.

Table 3. Calculated Excitation Energy (λ), Oscillator Strength (f), Main Orbital Contribution and Charge Characters of the Lowest Singlet and Triplet Excited States for the Optimized Ground-State Geometries of Ir(III) Complexes 1, 3, and 4, at PBE1PBE/6-31G (LANL2DZ with ECP for Ir) Level with PCM for Modeling the CH₂Cl₂ Solvent^a**

	state	λ (nm)	f	orbital contribution (>20%)	assignment
1	S ₁	450	0.0056	HOMO → LUMO+1 (70%) HOMO → LUMO (23%)	MLCT (24%), LLCT, ILCT, LC
	T ₁	584	0	HOMO → LUMO (52%) HOMO–1 → LUMO (30%)	MLCT (16%), LLCT, ILCT, LC
3	S ₁	490	0.0091	HOMO → LUMO+1 (68%) HOMO → LUMO (28%)	MLCT (21%), LLCT, ILCT, LC
	T ₁	584	0	HOMO → LUMO+1 (43%) HOMO → LUMO (21%)	MLCT (16%), LLCT, ILCT, LC
4	S ₁	488	0.0220	HOMO → LUMO (91%)	MLCT (21%), LLCT, ILCT, LC
	T ₁	592	0	HOMO → LUMO (45%) HOMO–1 → LUMO (23%)	MLCT (13%), LLCT, ILCT, LC

^aThe percentage of MLCT character of each MO transition was calculated from the decrease in the electron distribution on Ir atom. Complete orbital contribution and their assignments were collated in Table S4.

transfer (¹MLCT) transition, while the shoulder that extended into the longer wavelength region was due to the spin-forbidden ³MLCT absorption. The metal-induced spin–orbit coupling effect allows these spin-forbidden states mixed with spin-allowed singlet states. Therefore, the excitations from these states to the ground state (S₀) are weakly allowed with low oscillator strengths.

Upon excitation, the first three bis-tridentate Ir(III) complexes 1–3, i.e., all those with L1²⁻ chelate, showed that the structured emission profile with first peak maximum occurred in a narrow regime between 592 and 598 nm, together with two more lower-energy shoulders, one at ~645 nm, while the second appeared at ~705 nm. Both the structured profile and the lowered radiative rate constant (k_{r}) of $1.31\text{--}2.2 \times 10^5 \text{ s}^{-1}$ suggest the dominance of the intraligand charge transfer (ILCT) and ligand-to-ligand charge transfer (LLCT) transition character, together with MLCT transition contribution at the excited state manifolds. Similarly,

complexes 4 and 5 display an analogous structured pattern, but with a more red-shifted 0–0 emission peak wavelength (cf. at 612 and 617 nm) and vibronic sidebands, revealing the strong influence of dimethoxyphenyl peripheral group at this 3,5-dimethoxyphenyl substituted L2²⁻ chelate.

2.3. Electrochemical Properties. The redox properties of complexes 1–5 were studied using cyclic voltammetry, to which their CV traces and numeric data are depicted in Figure S2 and Table 2. As can be seen, all oxidation and reduction peaks are reversible, among which the Ir(III) complex 1 shows the most positive oxidation potential at 0.53 V. Moreover, complex 2 shows a further cathodic shift to 0.46 V, due to the addition of two *t*-butyl substituent at A2⁻ ancillary. Subsequently, Ir(III) complexes 3, 4, and 5 show less positive oxidation potential at 0.30, 0.27, and 0.25 V respectively, due to the introduction of 3,5-dimethoxyphenyl substituent irrespective to their location, and this confirmed the metal-centered oxidation process.

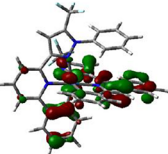
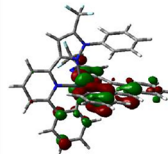
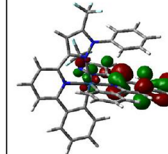
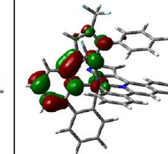
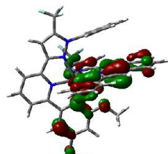
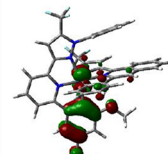
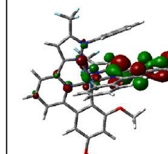
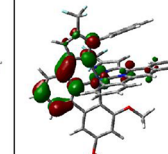
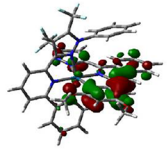
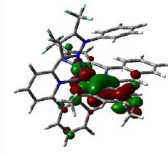
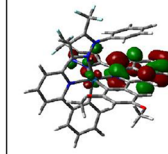
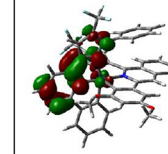
1				
	HOMO-1 (-6.04 eV) Ir (14%)	HOMO (-5.47 eV) Ir (30%)	LUMO (-1.84 eV) Ir (4%)	LUMO+1 (-1.75 eV) Ir (5%)
3				
	HOMO-1 (-5.71 eV) Ir (5%)	HOMO (-5.20 eV) Ir (27%)	LUMO (-1.76 eV) Ir (4%)	LUMO+1 (-1.72 eV) Ir (5%)
4				
	HOMO-1 (-5.89 eV) Ir (2%)	HOMO (-5.18 eV) Ir (26%)	LUMO (-1.82 eV) Ir (4%)	LUMO+1 (-1.65 eV) Ir (5%)

Figure 3. Key molecular orbitals calculated based on the optimized ground-state geometry (energy level and contribution from Ir atom for electron distribution are given in the parentheses), at PBE1PBE/6-31G** (LANL2DZ with ECP for Ir) level with PCM for modeling the CH_2Cl_2 solvent (for more orbitals see Figure S3 in the Supporting Information).

Alternatively, the reduction potentials also followed a similar trend as revealed in their oxidation potentials, among which the $\text{A}2^-$ ancillary of **2** and **5** induce more negative potentials in comparison to the $\text{A}1$ ancillary of **1** and **4**, whereas the $\text{L}2^{2-}$ chelate of **4** and **5** with 3,5-dimethoxy substituents is also capable to give more negative potentials with respect to both **1** and **2** with $\text{L}1^{2-}$ chelate. All these observations are consistent with the higher electron donating capability exerted by the *tert*-butyl and methoxy groups. After then, HOMO energy level of all Ir(III) complexes was calculated using the equation $\text{HOMO} = -(E_{\text{ox}} + 4.8)$ eV, while LUMO was calculated using the HOMO data and optical gap obtained from the onset of emission. All these data were listed in Table 2 for scrutiny.

2.4. Theoretical Investigation. The electronic structures of Ir(III) complexes **1**, **3**, and **4** were investigated in order to understand the nature of the absorption and emission bands and the effect of the ligand modification on the optical properties. Details of computational methods are described in the Experimental Section.

The calculated energy levels of HOMO and LUMO and their energy gap for complexes **1**, **3**, and **4** were tabulated in Table 2. The calculated HOMO energies for all three complexes showed the same trend as the observed values, that is, the HOMO energies of **3** and **4** (-5.20 eV and -5.18 eV) are higher than that of **1** (-5.47 eV). This is due to the addition of electron-donating methoxy groups compared to **1**. Furthermore, LUMO energies and the gap calculated by DFT are less physically meaningful than HOMO and the calculated gap should not be expected to be an approximation to the excitation energy. Instead, the excitation energy should be more properly described by, e.g., TD-DFT.

The calculated excitation energies in terms of wavelength and dominant orbital transitions for the lowest singlet- and triplet- excited states by TD-DFT are collated in Table 3, and the important frontier molecular orbitals are shown in Figure 3. The calculated excitation energies to the lowest singlet excited state (S_1) for complexes **1**, **3**, and **4** are 450, 490, and 488 nm, respectively, and were closely related to the observed values of the experimental absorption peaks shown in Figure 2 and Table 1 (452, 470, and 470 nm for **1**, **3**, and **4** respectively). This indicated the lowest Franck–Condon transition calculated by TD-DFT predicted a right trend for the lowest absorption peak of the investigated Ir(III) complexes. Moreover, the calculated energy of the lowest triplet excited state (T_1) on the Franck–Condon state (S_0 equilibrium geometry) for complexes **1**, **3**, and **4** are 584, 584, and 592 nm, respectively, which are well related to the experimental phosphorescence peaks (593 nm, 592 nm, 612 nm for **1**, **3**, and **4**, respectively).

However, the calculated energies of the T_1 excited state for **1**, **3**, and **4** based on the optimized triplet geometry are 793, 717, and 764 nm (see Table S3 in the Supporting Information), respectively, showing a different trend from the experimental phosphorescence peaks. This indicates the real structure of the emitting species is an intermediate between the calculated S_0 and T_1 equilibrium geometries for the investigated Ir(III) complexes. This finding has been reported extensively for other Ir(III) complexes and the main cause was reported as the lowest triplet state existed in a shallow anharmonic potential energy well.^{39,40}

LUMO of all three complexes is mainly localized at the $\text{L}n^{2-}$ chelate, while HOMO of all three complexes is more delocalized at the metal atom and both $\text{A}n^-$ and $\text{L}n^{2-}$ chelates.

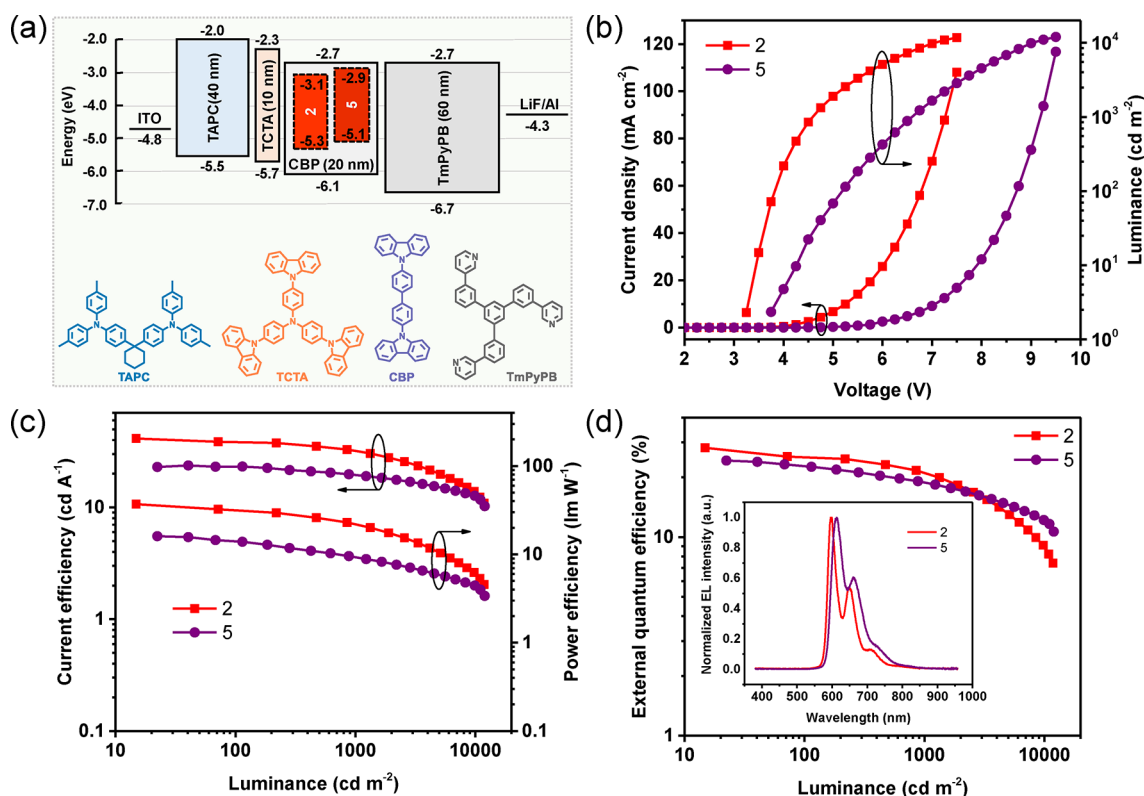


Figure 4. (a) Schematic device configuration, energy level diagram, and chemical structures of the employed materials for the OLEDs based on complexes **2** and **5** as emitters. (b) Current density–voltage–luminance (J – V – L) characteristics, (c) current efficiency and power efficiency versus luminance characteristics, and (d) external quantum efficiency versus luminance correlations of the devices (insert: EL spectra at 50 mA cm^{-2}).

The $T_1 \rightarrow S_0$ electronic excitation of **1** and **4** is mainly contributed by both HOMO–1 and HOMO to LUMO orbital transitions, whereas, that of **3** is mainly contributed by HOMO to both LUMO and LUMO+1 transition. The T_1 excited states of all three complexes show a mixed MLCT, ILCT, LLCT, and LC transition characters.

Moreover, the theoretical and experimental results show that adding electron donating 3,5-dimethoxyphenyl fragment on the $L1^{2-}$ ligand of **1** (forming $L2^{2-}$ of **4**) red-shifted the emission band, while adding 3,5-dimethoxyphenyl fragment at the $A1^-$ ligand of **1** (forming $A3^-$ of **3**) affected negligibly on the emission wavelength, i.e., failed to show the expected redshift. Note that **4** has both HOMO and LUMO localized on 3,5-dimethoxyphenyl thus this group at $L2^{2-}$ ligand decreases notably the $\pi\pi^*$ transition energy, while **3** has no LUMO localization on 3,5-dimethoxyphenyl of $A3^-$, resulting a negligibly change in the emission wavelength. Moreover, emission quantum yield is also reduced to only 15% in **3** from nearly unitary in complexes **1** and **2**. From Table 1, it is clearly that this drop of emission quantum yield in complex **3** is associated with the increase of k_{nr} , which were reported for the vibronic coupling process or the thermal population to nonradiative metal-centered states of Ir(III) complexes.^{41–43}

2.5. Electroluminescent Properties. The high PLQYs of Ir(III) complexes **2** and **5** inspired us to further investigate their EL properties. Thus, the red-emitting OLEDs with the following structure were fabricated: indium tin oxide (ITO)/4,4'-(cyclohexane-1,1-diyl)bis(*N,N*-di-*p*-tolylaniline) (TAPC, 40 nm)/tris(4-(9*H*-carbazol-9-yl)phenyl)amine (TCTA, 10 nm)/5 wt % of **2** or **5** doped in 4,4'-di(9*H*-carbazol-9-yl)-1,1'-biphenyl (CBP, 20 nm)/3,3'-(5'-(3-(pyridin-3-yl)-

phenyl)-[1,1':3',1''-terphenyl]-3,3''-diyl)dipyridine (TmPyPB, 60 nm)/LiF (1 nm)/Al (100 nm), in which the CBP host codeposited with 5 wt % of Ir(III) complex was constituted the emitting layer (EML). TAPC, TmPyPB and TCTA were employed as the hole-transporting layer (HTL), electron-transporting layer (ETL) and exciton-blocking layer, respectively. The schematic device structure, the energy diagram along with the corresponding molecular structures of these functional materials used in the device are depicted in Figure 4a.

The OLEDs using these Ir(III) complexes as dopants emit bright red emission with Commission Internationale de l'Éclairage (CIE) coordinates (0.63, 0.37) and (0.66, 0.34) for **2** and **5**, respectively. Besides, the EL spectra of all studied devices (Figure 4d) exhibit similar profile to their corresponding PL spectra, without any emission derived from the CBP host or any adjacent layer, indicating efficient energy transfer from host to the Ir(III) dopant and well confinement of the electron-generated excitons within the EML. Current density–voltage–luminance (J – V – L) characteristics of these devices are shown in Figure 4b. Complex **2**-based device shows better J – V characteristics with turn-on voltages (V_{on} , defined as the voltage at a brightness of 1 cd m^{-2}) below 3.5 V and low operation voltage (at a brightness of 100 cd m^{-2}) around 3.9 V. In contrast, the device of **5** exhibits a lowered current density at the same driving voltage, which can be explained by the carrier trapping effect caused by the much shallower HOMO levels relative to that of the CBP host. The efficiency–luminance curves of the investigated devices are depicted in parts c and d of Figure 4, and corresponding numeric data are summarized in Table 4. In general, the device based on **2**

Table 4. EL Performance of the OLEDs Based on Complexes 2 and 5

dopant	V_{on}^a [V]	EQE^b [%]	C^b [$cd\ A^{-1}$]	PE^b [$lm\ W^{-1}$]	λ_{max}^c [nm]	$CIE(x,y)^c$
2	<3.5	28.17/21.16	41.25/32.14	37.03/22.07	598	0.63, 0.37
5	<4.0	24.29/18.88	23.7/19.51	16.04/9.32	613	0.66, 0.34

^aTurn on voltages at $1\ cd\ m^{-2}$; ^bOrder of measured efficiency values: maximum, then values at $1000\ cd\ m^{-2}$; ^cData recorded at $50\ mA\ cm^{-2}$.

achieved excellent performance with a maximum external quantum efficiency (EQE_{max}) of 28.17%, a maximum current efficiency (CE_{max}) of $41.25\ cd\ A^{-1}$, and a maximum power efficiency (PE_{max}) of $37.03\ lm\ W^{-1}$, respectively. These efficiency are comparable to the state-of-the-art values for the Ir(III) complex-based red PhOLEDs.^{44–53} By contrast, the device based on 5 exhibits slightly lowered peak efficiency with an EQE_{max} of 24.29%, a CE_{max} of $23.7\ cd\ A^{-1}$ and a PE_{max} of $16.04\ lm\ W^{-1}$. However, it is worth noting that the efficiency roll-off of this device is much lower than that of 2 based device at high brightness, especially above $3000\ cd\ m^{-2}$, presumably due to the relatively higher radiative transition rate constant of 5.

3. CONCLUSION

In summary, a series of red-emitting bis-tridentate Ir(III) phosphors were synthesized and characterized by spectroscopic, structural and electrochemical methods, and by DFT and TD-DFT calculations. The employed structural modification involves addition of bulky substituents (e.g., a phenyl group at chelate A1[−], a pair of *tert*-butyl substituents at the chelate A2[−] with an intention to reduce intermolecular stacking interactions, and even addition of two electron donating methoxy groups in either A3[−] or L2^{2−} for possible red-shifting of emission wavelength. Photophysical and DFT and TD-DFT analyses demonstrate that the T₁ excited state of all investigated Ir(III) complexes show a mixed MLCT, ILCT, LLCT and LC transition character, as confirmed by the nearly unitary quantum yields (except 3), structured emission pattern, and relatively high radiative rate (k_r) of $(1.31–2.7) \times 10^5\ s^{-1}$. The poor quantum yield of 3 is due to the facilitation of the nonradiative decay in comparison to the radiative process. Red-emitting OLED devices were fabricated using representative Ir(III) complexes 2 and 5 as the dopant emitters. Both of them showed very high efficiency and significantly reduced roll-off at high luminance, among which complex 2 gives the best performances with maximum efficiencies of 28.17%, $41.25\ cd\ A^{-1}$, and $37.03\ lm\ W^{-1}$, and $CIE_{xy} = 0.63, 0.37$ at $50\ mA\ cm^{-2}$. These observations confirmed a notion that both the bulky *tert*-butyl and perpendicular arranged phenyl groups have effectively boosted the performances of OLED devices. Moreover, even in absence of strong field carbene based chelating unit, which is the common building block of blue-emitting Ir(III) phosphors, the bis-tridentate Ir(III) architectures composed of only pyridine- and pyrazolate-based donors can still behave as efficient design of the red-emitting OLED phosphors.

4. EXPERIMENTAL SECTION

4.1. General Information and Materials. All reactions were performed under a nitrogen atmosphere and solvents were distilled from appropriate drying agents prior to use. Commercially available reagents were used without further purification unless otherwise stated. Both 4-(*tert*-butyl)-2-(3-(*tert*-butyl)phenyl)-6-(1-phenyl-5-(trifluoromethyl)-1H-pyrazol-3-yl)pyridine (A2H) and 2-(3,5-dimethoxyphenyl)-6-(1-phenyl-5-(trifluoromethyl)-1H-pyrazol-3-yl)pyridine

(A3H) were prepared using the method established for A1H, while 3-(3,5-dimethoxyphenyl)-1-(3-(trifluoromethyl)-1H-pyrazol-5-yl)-isoquinoline (L2H₂) was prepared using the method established for L1H₂.⁵⁴ ¹H and ¹⁹F NMR spectra were measured with a Varian Mercury-400 instrument. UV-vis absorption and emission spectra were recorded using the Hitachi (U-4100) spectrophotometer and the Edinburgh (FS920) fluorometer, respectively. The nanosecond time-resolved studies were performed using an Edinburgh FL 900 time-correlated single photon-counting (TCSPC) system. Cyclic voltammetry was measured using a Model 600E Electrochemical Analyzer, CH Instruments. The elemental analysis was carried out on a Heraeus CHN-O Rapid Elementary Analyzer. Mass spectra were recorded on a JMS-T200GC AccuTOF GCx instrument operating in low resolution electron impact (LREI) or fast atom bombardment (FAB) mode.

4.1.1. Synthesis of Complex 1. A mixture of IrCl₃·3H₂O (100 mg, 0.28 mmol) and pz^{ph}pyphH (A1H, 102 mg, 0.28 mmol) in 25 mL of ethanol was heated at 110 °C for 12 h. After removal of ethanol, the pz^{iq}phH₂ (L1H₂, 96 mg, 0.28 mmol) and NaOAc (465 mg, 5.67 mmol) were dissolved in 20 mL of decalin and refluxed for 48 h. Next, the solvent was removed under vacuum and residue was dissolved in CH₂Cl₂. The solution was washed with deionized water, dried over anhydrous MgSO₄, and stripped to dryness. Further purification was conducted by silica gel column chromatography eluting with a 1:2 mixture of ethyl acetate and hexane, affording an orange red [Ir(A1)(L1)] (93 mg, 0.11 mmol); yield: 39%. Relevant bis-tridentate Ir(III) complexes 2–5 were synthesized using similar experimental procedures.

4.1.2. Selected Spectroscopic Data of 1. ¹H NMR (400 MHz, acetone-*d*₆): δ 8.67 (d, $J = 9.3\ Hz$, 1H), 8.31 (d, $J = 7.8\ Hz$, 1H), 8.16–8.09 (m, 3H), 8.04 (t, $J = 8.0\ Hz$, 1H), 7.98 (s, 1H), 7.84–7.74 (m, 2H), 7.70 (d, $J = 7.7\ Hz$, 1H), 7.67 (d, $J = 7.8\ Hz$, 1H), 7.43 (s, 1H), 6.87–6.76 (m, 3H), 6.72 (t, $J = 7.5\ Hz$, 1H), 6.66 (t, $J = 7.3\ Hz$, 1H), 6.52 (t, $J = 7.5\ Hz$, 2H), 6.45 (d, $J = 6.7\ Hz$, 2H), 6.01 (d, $J = 7.5\ Hz$, 1H), 5.80 (d, $J = 7.7\ Hz$, 1H). ¹⁹F NMR (376 MHz, acetone): δ −59.85 (s, 3F), −60.28 (s, 3F). MS [FAB]: m/z 894.2, M⁺. Anal. Calcd for C₄₀H₂₃F₆IrN₆: C, 53.75; H, 2.59; N, 9.40. Found: C, 53.93; H, 2.57; N, 9.54.

4.1.3. Selected Crystal Data of 1. C₄₀H₂₃F₆IrN₆; M = 894.84; monoclinic; space group = P2₁/n; $a = 13.5264(3)$, $b = 17.4386(4)$, and $c = 14.0191(3)$ Å; $\beta = 90.0487(6)^\circ$; $V = 3306.84(13)$ Å³; $Z = 4$; $\rho_{calcd} = 1.844\ Mg\ m^{-3}$; $F(000) = 1744$; crystal size = $0.320 \times 0.134 \times 0.108\ mm^3$; $\lambda(Mo\ K\alpha) = 0.71073\ \text{Å}$; $T = 150(2)\ K$; $\mu = 4.113\ mm^{-1}$; 27203 reflections collected, 9617 independent reflections ($R_{int} = 0.0334$), restrain/parameter = 0/478, GOF = 1.034, final $R_1 [I > 2\sigma(I)] = 0.0224$, and wR_2 (all data) = 0.044; Largest difference peak and hole = 0.712 and −0.593 e·Å^{−3}.

Complex 2 was isolated as orange red [Ir(A2)(L1)], yield: 83%. Selected spectroscopic data follow. ¹H NMR (400 MHz, acetone-*d*₆): δ 8.70–8.65 (m, 1H), 8.47 (d, $J = 1.7\ Hz$, 1H), 8.25 (d, $J = 1.7\ Hz$, 1H), 8.14 (s, 1H), 8.13–8.10 (m, 1H), 8.08 (s, 1H), 7.83–7.76 (m, 3H), 7.72 (dd, $J = 7.8, 1.2\ Hz$, 1H), 7.44 (s, 1H), 6.85 (td, $J = 7.5, 1.2\ Hz$, 1H), 6.80 (m, 2H), 6.67 (td, $J = 7.3, 1.3\ Hz$, 1H), 6.62 (dd, $J = 8.1, 2.1\ Hz$, 1H), 6.53 (tt, $J = 7.6, 1.1\ Hz$, 1H), 6.44 (d, $J = 7.2\ Hz$, 2H), 6.06 (dd, $J = 7.4, 1.2\ Hz$, 1H), 5.73 (d, $J = 8.1\ Hz$, 1H), 1.65 (s, 9H), 1.15 (s, 9H). ¹⁹F NMR (376 MHz, acetone): δ −59.86 (s, 3F), −60.20 (s, 3F). MS [FAB]: m/z 1006.3, M⁺. Anal. Calcd for C₄₈H₃₉F₆IrN₆: C, 57.30; H, 3.91; N, 8.35. Found: C, 57.67; H, 3.84; N, 8.63.

Complex 3 was isolated as orange red [Ir(A3)(L1)], yield: 43%. Selected spectroscopic data follow. ¹H NMR (400 MHz, acetone-*d*₆): δ 8.62 (d, $J = 7.7\ Hz$, 1H), 8.22 (d, $J = 7.6\ Hz$, 1H), 8.15 (d, $J = 8.1\ Hz$, 1H), 8.07 (d, $J = 7.4\ Hz$, 1H), 8.02 (s, 1H), 7.96 (s, 2H), 7.75 (m,

2H), 7.67 (d, $J = 7.6$ Hz, 1H), 7.41 (s, 1H), 6.99 (s, 1H), 6.81 (d, $J = 7.1$ Hz, 3H), 6.66 (t, $J = 7.2$ Hz, 1H), 6.52 (t, $J = 7.4$ Hz, 2H), 6.43 (s, 1H), 5.93 (d, $J = 7.3$ Hz, 1H), 5.72 (s, 1H), 3.65 (s, 3H), 2.55 (s, 3H). ^{19}F NMR (376 MHz, acetone): δ -59.87 (s, 3F), -60.09 (s, 3F). MS [FAB]: m/z 954.2, M^+ . Anal. Calcd for $\text{C}_{42}\text{H}_{27}\text{F}_6\text{IrN}_6\text{O}_2$: C, 52.88; H, 2.85; N, 8.81. Found: C, 53.11; H, 2.69; N, 8.87.

Complex **4** was isolated as red [Ir(A1)(L2)], yield: 45%. Spectroscopic data follow. ^1H NMR (400 MHz, acetone- d_6): δ 8.66 (d, $J = 8.4$ Hz, 1H), 8.23 (d, $J = 7.4$ Hz, 1H), 8.11 (m, 3H), 8.05 (s, 1H), 8.01 (d, $J = 7.8$ Hz, 1H), 7.95 (s, 1H), 7.79–7.76 (m, 2H), 7.62 (d, $J = 7.6$ Hz, 1H), 7.43 (s, 1H), 7.04 (s, 1H), 6.79 (s, 2H), 6.70 (t, $J = 7.3$ Hz, 1H), 6.56 (t, $J = 7.5$ Hz, 1H), 6.54–6.49 (m, 1H), 6.46 (d, $J = 6.8$ Hz, 1H), 5.90 (s, 1H), 5.74 (d, $J = 7.5$ Hz, 1H), 3.77 (s, 3H), 3.04 (d, $J = 8.5$ Hz, 3H). ^{19}F NMR (376 MHz, acetone): δ -59.70 (s, 3F), -60.22 (s, 3F). MS [FAB]: m/z 954.2, M^+ . Anal. Calcd for $\text{C}_{42}\text{H}_{27}\text{F}_6\text{IrN}_6\text{O}_2$: C, 52.88; H, 2.85; N, 8.81. Found: C, 52.77; H, 2.84; N, 8.81.

Complex **5** was isolated as red [Ir(A2)(L2)], yield: 80%. Selected spectroscopic data follow. ^1H NMR (400 MHz, acetone- d_6): δ 8.68–8.63 (m, 1H), 8.38 (s, 1H), 8.17–8.05 (m, 3H), 8.02 (s, 1H), 7.82–7.70 (m, 3H), 7.42 (s, 1H), 7.05 (s, 1H), 6.78 (t, $J = 7.3$ Hz, 2H), 6.61 (dd, $J = 8.0, 1.6$ Hz, 1H), 6.55 (t, $J = 7.5$ Hz, 1H), 6.43 (d, $J = 7.1$ Hz, 2H), 5.90 (s, 1H), 5.65 (d, $J = 8.0$ Hz, 1H), 3.77 (s, 3H), 3.04 (s, 3H), 1.65 (s, 9H), 1.15 (s, 9H). ^{19}F NMR (376 MHz, acetone): δ -59.71 (s, 3F), -60.11 (s, 3F). MS [FAB]: m/z 1066.3, M^+ . Anal. Calcd for $\text{C}_{50}\text{H}_{43}\text{F}_6\text{IrN}_6\text{O}_2$: C, 56.33; H, 4.07; N, 7.88. Found: C, 56.49; H, 3.82; N, 8.05.

4.2. Procedures for Theoretical Calculation. The electronic structure and electronic excitations of Ir(III) complexes **1**, **3**, and **4** were investigated by methods based on DFT^{55,56} and TD-DFT.^{57–59} The equilibrium S_0 geometries of complexes **1**, **3**, and **4** were optimized based on the X-ray structure of **1** (cf. Table S1 of Supporting Information). Both the geometry optimization and TD-DFT calculations were performed with the PBE1PBE^{60,61} functional combined with the polarizable continuum model (PCM)^{62–65} to include solvent effects of CH_2Cl_2 , using Gaussian 09 codes.⁶⁶ The 6-31G(d,p)⁶⁷ basis set was used for light elements such as hydrogen, carbon, nitrogen, oxygen, and fluorine, while the LANL2DZ⁶⁸ basis set with the Los Alamos National Laboratory (LANL)⁶⁹ effective core potentials (ECPs) was used for iridium. Mulliken population analysis was used to calculate the contribution from Ir atom for the electron distribution of each molecular orbital, the decrease of which in a molecular orbital transition was used to estimate the percentage of MLCT character. The T_1 geometry was optimized by unrestricted DFT based on equilibrium S_0 geometries. The results of benchmarking calculations using different functionals for geometry optimization and electronic excitations were listed in Tables S1 and S2, respectively.

4.3. OLED Device Fabrication and Measurement. Devices were fabricated on ITO-coated glass substrates with a sheet resistance of $15 \Omega \text{ sq}^{-1}$. Before device fabrication, ITO substrates were swabbed with Decon-90 solution and cleaned with deionized water, dried in an oven at 120°C , and treated with UV-ozone for 20 min before transferring into deposition chamber. All the organic materials, Liq, and Al were deposited at the rate of 1–2, 0.1, and $5 \text{ \AA} \cdot \text{s}^{-1}$, respectively, with a base pressure of 10^{-6} Torr. The current–voltage characteristics were measured using a Keithley 2400 source meter. Electroluminescence spectra were collected using a photonic multichannel analyzer PMA-12 (Hamamatsu C10027–01), which can detect in the spectral region 200–950 nm. All the measurements were carried out under ambient atmosphere at room temperature.

■ ASSOCIATED CONTENT

Supporting Information

The Supporting Information is available free of charge on the ACS Publications website at DOI: 10.1021/acs.inorgchem.9b01383.

Detailed synthetic procedures of chelates, original electrochemical data, and benchmarking and detailed

results of (TD-)DFT calculations including the Cartesian coordinates of the optimized ground-state geometries of the three studied Ir(III) metal complexes (PDF)

Accession Codes

CCDC 1908679 contains the supplementary crystallographic data for this paper. These data can be obtained free of charge via www.ccdc.cam.ac.uk/data_request/cif, or by emailing data_request@ccdc.cam.ac.uk, or by contacting The Cambridge Crystallographic Data Centre, 12 Union Road, Cambridge CB2 1EZ, UK; fax: +44 1223 336033.

■ AUTHOR INFORMATION

Corresponding Authors

* (Y.C.) E-mail: yunchi@cityu.edu.hk.

* (C.-S.L.) E-mail: apcslee@cityu.edu.hk.

* (X.Z.) E-mail: x.zhou6@uq.edu.au.

* (A.K.-Y.J.) E-mail: alexjen@cityu.edu.hk.

ORCID

Chun-Sing Lee: 0000-0001-6557-453X

Xiuwen Zhou: 0000-0002-7449-9380

Alex K.-Y. Jen: 0000-0002-9219-7749

Yun Chi: 0000-0002-8441-3974

Author Contributions

[†]These authors had equal contributions.

Notes

The authors declare no competing financial interest.

■ ACKNOWLEDGMENTS

This work was supported by the funding from Ministry of Science and Technology (MOST), featured areas research program within the framework of the Higher Education Sprout Project administrated by Ministry of Education (MOE) of Taiwan, and City University of Hong Kong, Hong Kong SAR. Single crystal X-ray structural analysis was conducted by Dr. G.-H. Lee of Instrumentation Center, National Taiwan University. X.Z. is supported by a University of Queensland Development Research Fellowship and a computation grant (rw25) from the National Computational Infrastructure of Australia.

■ REFERENCES

- (1) Tang, C. W.; VanSlyke, S. A. Organic electroluminescent diodes. *Appl. Phys. Lett.* **1987**, *51*, 913–915.
- (2) Tagare, J.; Vaidyanathan, S. Recent development of phenanthroimidazole-based fluorophores for blue organic light-emitting diodes (OLEDs): an overview. *J. Mater. Chem. C* **2018**, *6*, 10138–10173.
- (3) Chou, P.-T.; Chi, Y. Phosphorescent dyes for organic light-emitting diodes. *Chem. - Eur. J.* **2007**, *13*, 380–395.
- (4) Xiang, H.; Cheng, J.; Ma, X.; Zhou, X.; Chruma, J. J. Near-infrared phosphorescence: materials and applications. *Chem. Soc. Rev.* **2013**, *42*, 6128–6185.
- (5) Sasabe, H.; Kido, J. Development of high performance OLEDs for general lighting. *J. Mater. Chem. C* **2013**, *1*, 1699–1707.
- (6) Chi, Y.; Tong, B.; Chou, P.-T. Metal Complexes with Pyridyl Azolates: Design, Preparation and Applications. *Coord. Chem. Rev.* **2014**, *281*, 1–25.
- (7) Yang, X.; Zhou, G.; Wong, W.-Y. Functionalization of phosphorescent emitters and their host materials by main-group elements for phosphorescent organic light-emitting devices. *Chem. Soc. Rev.* **2015**, *44*, 8484–8575.

- (8) Li, T.-Y.; Wu, J.; Wu, Z.-G.; Zheng, Y.-X.; Zuo, J.-L.; Pan, Y. Rational design of phosphorescent iridium(III) complexes for emission color tunability and their applications in OLEDs. *Coord. Chem. Rev.* **2018**, *374*, 55–92.
- (9) Uoyama, H.; Goushi, K.; Shizu, K.; Nomura, H.; Adachi, C. Highly efficient organic light-emitting diodes from delayed fluorescence. *Nature* **2012**, *492*, 234–238.
- (10) Adachi, C. Third-generation organic electroluminescence materials. *Jpn. J. Appl. Phys.* **2014**, *53*, No. 060101.
- (11) Wong, M. Y.; Zysman-Colman, E. Purely Organic Thermally Activated Delayed Fluorescence Materials for Organic Light-Emitting Diodes. *Adv. Mater.* **2017**, *29*, 1605444.
- (12) Kim, J. H.; Yun, J. H.; Lee, J. Y. Recent Progress of Highly Efficient Red and Near-Infrared Thermally Activated Delayed Fluorescent Emitters. *Adv. Opt. Mater.* **2018**, *6*, 1800255.
- (13) Cai, X.; Su, S.-J. Marching Toward Highly Efficient, Pure-Blue, and Stable Thermally Activated Delayed Fluorescent Organic Light-Emitting Diodes. *Adv. Funct. Mater.* **2018**, *28*, 1802558.
- (14) Chi, Y.; Chang, T.-K.; Ganesan, P.; Rajakannu, P. Emissive Bis-Tridentate Ir(III) Metal Complexes: Tactics. *Coord. Chem. Rev.* **2017**, *346*, 91–100.
- (15) Kim, K.-H.; Moon, C.-K.; Lee, J.-H.; Kim, S.-Y.; Kim, J.-J. Highly Efficient Organic Light-Emitting Diodes with Phosphorescent Emitters Having High Quantum Yield and Horizontal Orientation of Transition Dipole Moments. *Adv. Mater.* **2014**, *26*, 3844–3847.
- (16) Lee, T.; Caron, B.; Stroet, M.; Huang, D. M.; Burn, P. L.; Mark, A. E. The molecular origin of anisotropic emission in an organic light-emitting diode. *Nano Lett.* **2017**, *17*, 6464–6468.
- (17) Wilkinson, A. J.; Puschmann, H.; Howard, J. A. K.; Foster, C. E.; Williams, J. A. G. Luminescent Complexes of Iridium(III) Containing N[∧]C[∧]N-Coordinating Terdentate Ligands. *Inorg. Chem.* **2006**, *45*, 8685–8699.
- (18) Williams, J. A. G.; Wilkinson, A. J.; Whittle, V. L. Light-emitting iridium complexes with tridentate ligands. *Dalton Trans.* **2008**, 2081–2099.
- (19) Esteruelas, M. A.; Gómez-Bautista, D.; López, A. M.; Oñate, E.; Tsai, J.-Y.; Xia, C. η^1 -Arene Complexes as Intermediates in the Preparation of Molecular Phosphorescent Iridium(III) Complexes. *Chem. - Eur. J.* **2017**, *23*, 15729–15737.
- (20) Kuo, H.-H.; Zhu, Z.-L.; Lee, C.-S.; Chen, Y.-K.; Liu, S.-H.; Chou, P.-T.; Jen, A. K.-Y.; Chi, Y. Bis-tridentate Iridium(III) Phosphors with Very High Photostability and Fabrication of Blue-Emitting OLEDs. *Adv. Sci.* **2018**, *5*, 1800846.
- (21) Chi, Y.; Wu, K.-L.; Wei, T.-C. Ruthenium and Osmium Complexes That Bear Functional Azolate Chelates for Dye-Sensitized Solar Cells. *Chem. - Asian J.* **2015**, *10*, 1098–1115.
- (22) Chou, C.-C.; Wu, K.-L.; Chi, Y.; Hu, W.-P.; Yu, S. J.; Lee, G.-H.; Lin, C.-L.; Chou, P.-T. Ru(II) Sensitizers with Heteroleptic Tridentate Chelates for Dye-Sensitized Solar Cells. *Angew. Chem., Int. Ed.* **2011**, *50*, 2054–2058.
- (23) Hsu, C.-W.; Ho, S.-T.; Wu, K.-L.; Chi, Y.; Liu, S.-H.; Chou, P.-T. Ru(II) sensitizers with a tridentate heterocyclic cyclometalate for dye-sensitized solar cells. *Energy Environ. Sci.* **2012**, *5*, 7549–7554.
- (24) Wu, K.-L.; Ho, S.-T.; Chou, C.-C.; Chang, Y.-C.; Pan, H.-A.; Chi, Y.; Chou, P.-T. Engineering of Osmium(II)-Based Light Absorbers for Dye-Sensitized Solar Cells. *Angew. Chem., Int. Ed.* **2012**, *51*, 5642–5646.
- (25) Chou, C.-C.; Hu, F.-C.; Yeh, H.-H.; Wu, H.-P.; Chi, Y.; Clifford, J. N.; Palomares, E.; Liu, S.-H.; Chou, P.-T.; Lee, G.-H. Highly Efficient Dye-Sensitized Solar Cells Based on Panchromatic Ruthenium Sensitizers with Quinolinylbipyridine Anchors. *Angew. Chem., Int. Ed.* **2014**, *53*, 178–183.
- (26) Chen, J.-L.; Wu, Y.-H.; He, L.-H.; Wen, H.-R.; Liao, J.; Hong, R. Iridium(III) Bis-tridentate Complexes with 6-(5-Trifluoromethylpyrazol-3-yl)-2,2'-bipyridine Chelating Ligands: Synthesis, Characterization, and Photophysical Properties. *Organometallics* **2010**, *29*, 2882–2891.
- (27) Tong, B.; Ku, H. Y.; Chen, I. J.; Chi, Y.; Kao, H.-C.; Yeh, C.-C.; Chang, C.-H.; Liu, S.-H.; Lee, G.-H.; Chou, P.-T. Heteroleptic Ir(III) Phosphors with Bis-Tridentate Chelating Architecture for High Efficiency OLEDs. *J. Mater. Chem. C* **2015**, *3*, 3460–3471.
- (28) Kuei, C.-Y.; Liu, S.-H.; Chou, P.-T.; Lee, G.-H.; Chi, Y. Room Temperature Blue Phosphorescence; A Combined Experimental and Theoretical Study on the Bis-tridentate Ir(III) Metal Complexes. *Dalton Trans.* **2016**, *45*, 15364–15373.
- (29) Lin, J.; Chau, N.-Y.; Liao, J.-L.; Wong, W.-Y.; Lu, C.-Y.; Sie, Z.-T.; Chang, C.-H.; Fox, M. A.; Low, P. J.; Lee, G.-H.; Chi, Y. Bis-Tridentate Iridium(III) Phosphors Bearing Functional 2-Phenyl-6-(imidazol-2-ylidene)pyridine and 2-(Pyrazol-3-yl)-6-phenylpyridine Chelates for Efficient OLEDs. *Organometallics* **2016**, *35*, 1813–1824.
- (30) Roesch, K. R.; Larock, R. C. Synthesis of Isoquinolines and Pyridines by the Palladium/Copper-Catalyzed Coupling and Cyclization of Terminal Acetylenes and Unsaturated Imines: The Total Synthesis of Decumbenine B. *J. Org. Chem.* **2002**, *67*, 86–94.
- (31) Jeganathan, M.; Pitchumani, K. Synthesis of substituted isoquinolines via iminoalkyne cyclization using Ag(I) exchanged K10-montmorillonite clay as a reusable catalyst. *RSC Adv.* **2014**, *4*, 38491–38497.
- (32) Lin, J.; Wang, Y.; Gnanasekaran, P.; Chiang, Y.-C.; Yang, C.-C.; Chang, C.-H.; Liu, S.-H.; Lee, G.-H.; Chou, P.-T.; Chi, Y.; Liu, S.-W. Unprecedented Homoleptic Bis-Tridentate Iridium(III) Phosphors: Facile, Scaled-Up Production, and Superior Chemical Stability. *Adv. Funct. Mater.* **2017**, *27*, 1702856.
- (33) Costa, R. D.; Orti, E.; Bolink, H. J.; Graber, S.; Housecroft, C. E.; Constable, E. C. Light-emitting electrochemical cells based on a supramolecularly-caged phenanthroline-based iridium complex. *Chem. Commun.* **2011**, *47*, 3207–3209.
- (34) Li, P.; Shan, G.-G.; Cao, H.-T.; Zhu, D.-X.; Su, Z.-M.; Jitchati, R.; Bryce, M. R. Intramolecular π Stacking in Cationic Iridium(III) Complexes with Phenyl-Functionalized Cyclometalated Ligands: Synthesis, Structure, Photophysical Properties, and Theoretical Studies. *Eur. J. Inorg. Chem.* **2014**, *2014*, 2376–2382.
- (35) Qu, X.; Liu, Y.; Si, Y.; Wu, X.; Wu, Z. A theoretical study on supramolecularly-caged positively charged iridium(III) 2-pyridyl azolate derivatives as blue emitters for light-emitting electrochemical cells. *Dalton Trans.* **2014**, *43*, 1246–1260.
- (36) Housecroft, C. E.; Constable, E. C. Over the LEC rainbow: Colour and stability tuning of cyclometalated iridium(III) complexes in light-emitting electrochemical cells. *Coord. Chem. Rev.* **2017**, *350*, 155–177.
- (37) Namanga, J.; Gerlitzki, N.; Smetana, V.; Mudring, A.-V. Supramolecularly-caged green emitting ionic Ir(III)-based complex with fluorinated C[∧]N ligands and its application in light emitting electrochemical cells. *ACS Appl. Mater. Interfaces* **2018**, *10*, 11026–11036.
- (38) Qu, Z.-Z.; Gao, T.-B.; Wen, J.; Rui, K.; Ma, H.; Cao, D.-K. Cyclometalated Ir(III) complexes [Ir(tpy)(bbibH₂)Cl][PF₆] and [Ir(tpy)(bmbib)Cl][PF₆]: intramolecular π - π interactions leading to facile synthesis and enhanced luminescence. *Dalton Trans.* **2018**, *47*, 9779–9786.
- (39) Younker, J. M.; Dobbs, K. D. Correlating Experimental Photophysical Properties of Iridium(III) Complexes to Spin–Orbit Coupled TDDFT Predictions. *J. Phys. Chem. C* **2013**, *117*, 25714–25723.
- (40) Jansson, E.; Norman, P.; Minaev, B.; Ågren, H. Evaluation of low-scaling methods for calculation of phosphorescence parameters. *J. Chem. Phys.* **2006**, *124*, 114106.
- (41) Yersin, H.; Rausch, A. F.; Czerwieniec, R.; Hofbeck, T.; Fischer, T. The triplet state of organo-transition metal compounds. Triplet harvesting and singlet harvesting for efficient OLEDs. *Coord. Chem. Rev.* **2011**, *255*, 2622–2652.
- (42) Zhou, X.; Burn, P. L.; Powell, B. J. Bond Fission and Non-Radiative Decay in Iridium(III) Complexes. *Inorg. Chem.* **2016**, *55*, 5266–5273.
- (43) Zhou, X.; Powell, B. J. Nonradiative Decay and Stability of N-Heterocyclic Carbene Iridium(III) Complexes. *Inorg. Chem.* **2018**, *57*, 8881–8889.

- (44) Feng, Y.; Li, P.; Zhuang, X.; Ye, K.; Peng, T.; Liu, Y.; Wang, Y. A novel bipolar phosphorescent host for highly efficient deep-red OLEDs at a wide luminance range of 1000–10 000 cd m⁻². *Chem. Commun.* **2015**, *51*, 12544–12547.
- (45) Cui, L.-S.; Liu, Y.; Liu, X.-Y.; Jiang, Z.-Q.; Liao, L.-S. Design and Synthesis of Pyrimidine-Based Iridium(III) Complexes with Horizontal Orientation for Orange and White Phosphorescent OLEDs. *ACS Appl. Mater. Interfaces* **2015**, *7*, 11007–11014.
- (46) Li, G.; Feng, Y.; Peng, T.; Ye, K.; Liu, Y.; Wang, Y. Highly efficient, little efficiency roll-off orange-red electrophosphorescent devices based on a bipolar iridium complex. *J. Mater. Chem. C* **2015**, *3*, 1452–1456.
- (47) Shih, C.-H.; Rajamalli, P.; Wu, C.-A.; Hsieh, W.-T.; Cheng, C.-H. A Universal Electron-Transporting/Exciton-Blocking Material for Blue, Green, and Red Phosphorescent Organic Light-Emitting Diodes (OLEDs). *ACS Appl. Mater. Interfaces* **2015**, *7*, 10466–10474.
- (48) Kim, K.-H.; Liao, J.-L.; Lee, S. W.; Sim, B.; Moon, C.-K.; Lee, G.-H.; Kim, H. J.; Chi, Y.; Kim, J.-J. Crystal Organic Light-Emitting Diodes with Perfectly Oriented Non-Doped Pt-Based Emitting Layer. *Adv. Mater.* **2016**, *28*, 2526–2532.
- (49) Lee, J.-H.; Shin, H.; Kim, J.-M.; Kim, K.-H.; Kim, J.-J. Exciplex-Forming Co-Host-Based Red Phosphorescent Organic Light-Emitting Diodes with Long Operational Stability and High Efficiency. *ACS Appl. Mater. Interfaces* **2017**, *9*, 3277–3281.
- (50) Jiang, B.; Zhao, C.; Ning, X.; Zhong, C.; Ma, D.; Yang, C. Using Simple Fused-Ring Thieno[2,3-d]pyrimidine to Construct Orange/Red Ir(III) Complexes: High-Performance Red Organic Light-Emitting Diodes with EQEs up to Nearly 28%. *Adv. Opt. Mater.* **2018**, *6*, 1800108.
- (51) Wang, Y.-K.; Li, S.-H.; Wu, S.-F.; Huang, C.-C.; Kumar, S.; Jiang, Z.-Q.; Fung, M.-K.; Liao, L.-S. Tilted Spiro-Type Thermally Activated Delayed Fluorescence Host for ≈100% Exciton Harvesting in Red Phosphorescent Electronics with Ultralow Doping Ratio. *Adv. Funct. Mater.* **2018**, *28*, 1706228.
- (52) Yang, X.; Guo, H.; Liu, B.; Zhao, J.; Zhou, G.; Wu, Z.; Wong, W.-Y. Diarylboron-Based Asymmetric Red-Emitting Ir(III) Complex for Solution-Processed Phosphorescent Organic Light-Emitting Diode with External Quantum Efficiency above 28%. *Adv. Sci.* **2018**, *5*, 1701067.
- (53) Lu, G.-Z.; Su, n.; Yang, H.; Zhu, Q.; Zhang, W.-W.; Zheng, Y.; Zhou, L.; Zuo, J.-L.; Chen, Z.-X.; Zhang, H. Rapid room temperature synthesis of red iridium(III) complexes containing four-membered Ir-S-C-S chelating ring for highly efficient OLEDs with EQE over 30%. *Chem. Sci.* **2019**, *10*, 3535–3542.
- (54) Sloop, J. C.; Bumgardner, C. L.; Loehle, W. D. Synthesis of fluorinated heterocycles. *J. Fluorine Chem.* **2002**, *118*, 135–147.
- (55) Hohenberg, P.; Kohn, W. Inhomogeneous Electron Gas. *Phys. Rev.* **1964**, *136*, B864–B871.
- (56) Kohn, W.; Sham, L. J. Self-Consistent Equations Including Exchange and Correlation Effects. *Phys. Rev.* **1965**, *140*, A1133–A1138.
- (57) Runge, E.; Gross, E. K. U. Density-Functional Theory for Time-Dependent Systems. *Phys. Rev. Lett.* **1984**, *52*, 997–1000.
- (58) Casida, M. E.; Jamorski, C.; Casida, K. C.; Salahub, D. R. Molecular excitation energies to high-lying bound states from time-dependent density-functional response theory: Characterization and correction of the time-dependent local density approximation ionization threshold. *J. Chem. Phys.* **1998**, *108*, 4439.
- (59) Casida, M. E. Time-dependent density-functional theory for molecules and molecular solids. *J. Mol. Struct.: THEOCHEM* **2009**, *914*, 3–18.
- (60) Adamo, C.; Barone, V. Toward reliable density functional methods without adjustable parameters: The PBE0 model. *J. Chem. Phys.* **1999**, *110*, 6158–6170.
- (61) Ernzerhof, M.; Scuseria, G. E. Assessment of the Perdew-Burke-Ernzerhof exchange-correlation functional. *J. Chem. Phys.* **1999**, *110*, 5029–5036.
- (62) Miertuš, S.; Scrocco, E.; Tomasi, J. Electrostatic interaction of a solute with a continuum. A direct utilization of AB initio molecular potentials for the prevision of solvent effects. *Chem. Phys.* **1981**, *55*, 117–129.
- (63) Mennucci, B.; Tomasi, J. Continuum solvation models: A new approach to the problem of solute's charge distribution and cavity boundaries. *J. Chem. Phys.* **1997**, *106*, 5151–5158.
- (64) Barone, V.; Cossi, M. Quantum Calculation of Molecular Energies and Energy Gradients in Solution by a Conductor Solvent Model. *J. Phys. Chem. A* **1998**, *102*, 1995–2001.
- (65) Tomasi, J.; Mennucci, B.; Cammi, R. Quantum Mechanical Continuum Solvation Models. *Chem. Rev.* **2005**, *105*, 2999–3094.
- (66) Frisch, M. J.; Trucks, G. W.; Schlegel, H. B.; Scuseria, G. E.; Robb, M. A.; Cheeseman, J. R.; Scalmani, G.; Barone, V.; Mennucci, B.; Petersson, G. A.; Nakatsuji, H.; Caricato, M.; Li, X.; Hratchian, H. P.; Izmaylov, A. F.; Bloino, J.; Zheng, G.; Sonnenberg, J. L.; Hada, M.; Ehara, M.; Toyota, K.; Fukuda, R.; Hasegawa, J.; Ishida, M.; Nakajima, T.; Honda, Y.; Kitao, O.; Nakai, H.; Vreven, T.; Montgomery, J. A.; Peralta, J. E.; Ogliaro, F.; Bearpark, M.; Heyd, J. J.; Brothers, E.; Kudin, K. N.; Staroverov, V. N.; Kobayashi, R.; Normand, J.; Raghavachari, K.; Rendell, A.; Burant, J. C.; Iyengar, S. S.; Tomasi, J.; Cossi, M.; Rega, N.; Millam, J. M.; Klene, M.; Knox, J. E.; Cross, J. B.; Bakken, V.; Adamo, C.; Jaramillo, J.; Gomperts, R.; Stratmann, R. E.; Yazyev, O.; Austin, A. J.; Cammi, R.; Pomelli, C.; Ochterski, J. W.; Martin, R. L.; Morokuma, K.; Zakrzewski, V. G.; Voth, G. A.; Salvador, P.; Dannenberg, J. J.; Dapprich, S.; Daniels, A. D.; Farkas, Ö.; Foresman, J. B.; Ortiz, J. V.; Cioslowski, J.; Fox, D. J. *Gaussian 16*, Revision A03; Gaussian Inc.: Wallingford, CT, 2016.
- (67) Hariharan, P. C.; Pople, J. A. The influence of polarization functions on molecular orbital hydrogenation energies. *Theor. Chim. Acta* **1973**, *28*, 213–222.
- (68) Weigend, F.; Ahlrichs, R. Balanced basis sets of split valence, triple zeta valence and quadruple zeta valence quality for H to Rn: Design and assessment of accuracy. *Phys. Chem. Chem. Phys.* **2005**, *7*, 3297–3305.
- (69) Hay, P. J.; Wadt, W. R. Ab initio effective core potentials for molecular calculations. Potentials for K to Au including the outermost core orbitals. *J. Chem. Phys.* **1985**, *82*, 299–310.